RSC Advances

ROYAL SOCIETY OF CHEMISTRY

www.rsc.org/advances

PEGylated Gold Nanoprisms for Photothermal Therapy at Low Laser Power Density

Xingqun Ma,[a] Yuan Cheng,[a] Yong Huang,[a] Ying Tian,[b] Shouju Wang*[b] and Yingxia Chen*[a]

a. PLA Cancer Center of Nanjing Bayi Hospital, Nanjing 210002, China
b. Department of Medical Imaging, Jinling Hospital, School of Medicine, Nanjing University, Nanjing 210002, China

*Corresponding authors:
Yingxia Chen, M.D.
PLA Cancer Center of Nanjing Bayi Hospital, Nanjing 210002, China
E-mail: chenyingxiacsco@163.com

Shouju Wang, M.D.
Department of Medical Imaging, Jinling Hospital, School of Medicine, Nanjing University, Nanjing 210002, China
E-mail: shouju.wang@gmail.com

Abstract

This paper developed small-sized PEGylated gold nanoprisms (GNPs) to induce photothermal therapy at low laser power density. Upon irradiation of laser at low power density (2 W cm^{-2}), these PEGylated GNPs showed ultrahigh photothermal conversion efficacy ($\eta \approx 70\%$) and produced enough heat to kill human breast cancer cells.

1. Introduction

Photothermal therapy (PTT) has emerged as a promising way to treat cancer with minimal invasion and high selectivity.[1-9] An ideal nanostructure for PTT is expected to have the following features: 1) appropriate size between 10 to 100 nm.[10,11] Nanoparticles with size larger than 100 nm are more easily gulfed by reticuloendothelial system (RES), while those smaller than 10 nm excrete rapidly from kidney; 2) strong absorption in the near-infrared (NIR, λ = 650-900 nm) window, in which the laser has maximal penetration ability in tissues;[12] 3) high photothermal conversion efficacy to reduce the required laser power density[13] and 4) good biostability and biocompatibility with little to no toxicity to normal cells/tissues.[14,15]

Gold nanoprisms (GNPs) are a novel class of anisotropic gold nanoparticles having strong plasmon absorption that suitable for surface enhanced Raman spectroscopy (SERS).[16,17] However, the application of GNPs for PTT are rarely reported probably due to their relatively large size (> 100 nm) and low photothermal conversion efficacy.[18,19] Recently, Fuente and co-workers effectively ablated tumor cells using large-sized GNPs under a 1064 nm laser, however the required laser power density (30 W cm^{-2}) was rather high, which is far beyond the American National Standard Institute (ANSI) safety limit for skin exposure.[20,21]

Herein, we tested the possibility of performing PTT with small-sized GNPs (~50 nm) under low power density laser. We showed that the PEGylated GNPs have excellent biostability and biocompatibility. Under irradiation of NIR laser (650 nm), these PEGylated GNPs converted laser energy to heat efficiently, and induced massive tumor cells necrosis even when the laser power density was pretty low.

2. Experimental

2.1 Materials.

Hexadecyltrimethylammonium chloride (CTAC) was purchased from TCI. Potassium iodide (KI), L-ascorbic acid, Gold (III) chloride trihydrate, thiazolyl blue tetrazolium bromide (MTT), and dimethyl sulphoxide (DMSO) were purchased from Sigma Aldrich. Methoxy-PEG-thiol (mPEG-SH, M.W. ≈ 5000 Da) were purchased from Laysan Bio Inc.. LIVE/DEAD viability/cytotoxicity kit was purchased from Invitrogen. Ultrapure water was obtained from a Milli-Q system. All chemicals were used as received without further treatment.

2.2 Synthesis of CTAC-capped GNPs.

GNPs were prepared by a modified seed-less method.[16] In brief, 4.8 mL of 0.1 M CTAC was diluted in 24 mL pure water, followed by addition of 225 μL of 0.01 M KI, 240 μL of 25.4 mM $HAuCl_4$, and 61 μL of 0.1 M NaOH. Then 300 μL of 0.064 M ascorbic acid was added with moderate shaking. When the solution turned to colorless, 10 μL of 0.1 M NaOH was injected and the solution was rapidly shaken for 2-3 s.

2.3 PEGylation of CTAC-capped GNPs with mPEG-SH.

In a typical process, 30 mL of prepared CTAC-capped GNPs were purified by centrifugation and re-dispersed in 1 mL of ultrapure water. Then 250 μL of 4 mM PEG-SH was added, followed by addition of 9 mL of ultrapure water to a total volume of 10 mL. The reaction mixture was vortexed immediately and then incubated in an ultrasound bath for 30 min, followed by centrifuging at 7000 rpm for 10 min.

2.4 Characterization of GNPs.

Transmission electron microscopy (TEM) characterization was conducted using a JEOL JEM-2100 microscope (Japan) at 200 kV. The hydrodynamic diameter and surface charge of samples were obtained by a ZetaPALS analyzer (Brookhaven, USA). The absorbance of spectra were characterized using a Lambda 35 UV/vis spectrometer (PerkinElmer, USA).

2.5 Simulation using FDTD method.

For the simulation of plasmonic properties of GNPs, Lumerical FDTD solution of version 8.12.5 was used. The override mesh cell size was 1 x 1 x 1 nm^3. The dielectric constants of gold were taken from the preset material database (Johnson and Christy). A simulation area of 800 x 800 x 800 nm^3 surrounded by 12 perfectly matched layers (PMLs) was used. The wavelength of the total-field scattered-field (TFSF) source used in simulation ranged from 300 to 1100 nm. The light from TFSF source was set to be propagating along the z-axis with 90 degrees of polarization angle. Power monitors in the total field region and the scattered field region were used to determine the absorption cross-section and scattering cross-section, respectively. The PEG or CTAC layers were ignored and the background refractive index was set as 1.33. The extinction spectrum was calculated as the sum of the absorption and scattering spectra. The dimensions of GNPs were set as 55 nm in edge length and 20 nm in thickness.

2.6 Laser setup and temperature measurement.

For the NIR irradiation experiments, a continuous wave laser ($\lambda = 650 \pm 10$ nm) supplied by Beijing Hi-Tech Optoelectronics Co., Ltd was coupled with a custom-made fiber collimator. The spot size was calibrated to cover the top surface of quartz. The laser power density was adjusted to 2 W cm^{-2} by a laser power meter (Coherent, USA). The

temperature of solutions was monitored by a MAGNITY f15F1 infrared camera (Wuhan VST Light & Technology Co., Ltd, China) as shown in Figure S1.

2.7 Calculation of photothermal conversion efficacy.

The photothermal conversion efficacy of PEGylated GNPs was calculated using the following equation.

$$\eta = \frac{hS(T_{max} - T_{amb}) - Q_0}{I(1 - 10^{-A})}$$

Where h is heat transfer coefficient, S is the surface area, T_{max} is the equilibrium temperature, T_{amb} is the ambient temperature of the surroundings, Q_0 express heat absorbed by the quartz cell, I is the laser power, and A is the absorbance of PEGylated GNPs at 650 nm.

When the heat input is equal to the heat output, the hS can be calculated by the following equation:

$$hS = \frac{\sum_i m_i C_{p,i}}{\tau_s} \approx \frac{m_{H2O} C_{H2O}}{\tau_s}$$

Where τ_s is the a sample system time constant, m_{H2O} is the weight of water, and C_{H2O} is the specific heat capacity of water.

At the cooling stage:

$$t = -\tau_s ln\theta = -\tau_s ln \frac{T - T_{amb}}{T_{max} - T_{amb}}$$

Thus, the time constant τ_s can be determined by applying the linear time data from the cooling stage *vs* negative natural logarithm of driving force temperature.

2.8 Cell culture.

Human breast cancer cells (MCF-7 cells) were purchased from American tissue culture collection (ATCC) and cultured in DMEM with 10% fetal bovine serum and 1%

penicillin/streptomycin in a humidified incubator at 37 °C with 5% CO_2. Human breast basal epithelial cells (MCF-10A cells) was purchased from ATCC and cultured in mammary epithelial cell growth medium (MEBM) with 13 μg/mL bovine pituitary extract, 1 μg/mL hydrocortisone, 5 μg/mL insulin, 10 ng/mL epidermal growth factor, and 10 μg/mL cholera toxin in a humidified incubator at 37 °C with 5% CO_2.

2.9 *In vitro* PPT studies.

MCF-7 cells were cultured in 96-well plates and followed by addition of PEGylated GNPs suspended in DMEM. The final concentration of PEGylated GNPs was 2.5, 5, 10, 20, 40 and 80 μg/mL. The cells were incubated at 37 °C and 5% CO_2 overnight, washed by cold PBS for three times and followed by irradiation by a 761 nm laser at 2 W cm^{-2} for 10 min. The MTT assays were performed by previously reported procedure. [1] Cell live/dead staining was performed following the manufacturer's instruction (Invitrogen).

2.10 Biocompatibility studies.

MCF-10A cells were cultured in 96-well plates and followed by addition of PEGylated or CTAC-capped GNPs suspended in MEGM. The final concentration of GNPs was 2.5, 5, 10, 20, 40 and 80 μg/mL. The cells were incubated at 37 °C and 5% CO_2 overnight, washed by cold PBS for three times. the cell viability was determined by MTT assay as described in the previous section.

2.11 Hemolysis analysis.

Fresh human blood sample was washed three times by cold saline (0.9% sodium chloride). Then the red bold cells were carefully collected and diluted in saline and incubated with various concentration of PEGylated or CTAC-capped GNPs 37 °C for 2 h. The final concentration of GNPs was 3.1, 6.2, 12.5, 25, 50, 100, 200, and 400 μg/mL.

After that, the mixtures were centrifuged at 2000 rpm for 5 min, and 150 μL of the supernatant was transferred to a 96-well plate. The absorbance values of the supernatants at 490 nm were determined using a microplate reader with absorbance at 630 nm as a reference. Diluted red blood cells (RBCs) suspension incubated with saline or ultrawater was used as the negative or positive control.

The hemolysis activity was calculated using the following formula: (sample absorbance – negative control absorbance)/(positive control absorbance – negative control absorbance)× 100.

3. Results and discussion

3.1 Characterization of PEGylated GNPs

GNPs were synthesized following a method using hexadecyltrimethylammonium chloride (CTAC) as surfactant[16] and decorated with methoxy polyethylene glycol thiol (mPEG-SH, MW ≈ 5000) using a ligand exchange process. Figure 1a shows transmission electron microscopy (TEM) image of PEGylated GNPs with edge length of 55.6 ± 1.6 nm. Analysis of vertically oriented nanoparticles showed the average thickness of GNPs was around 20 nm (Figure 1b).

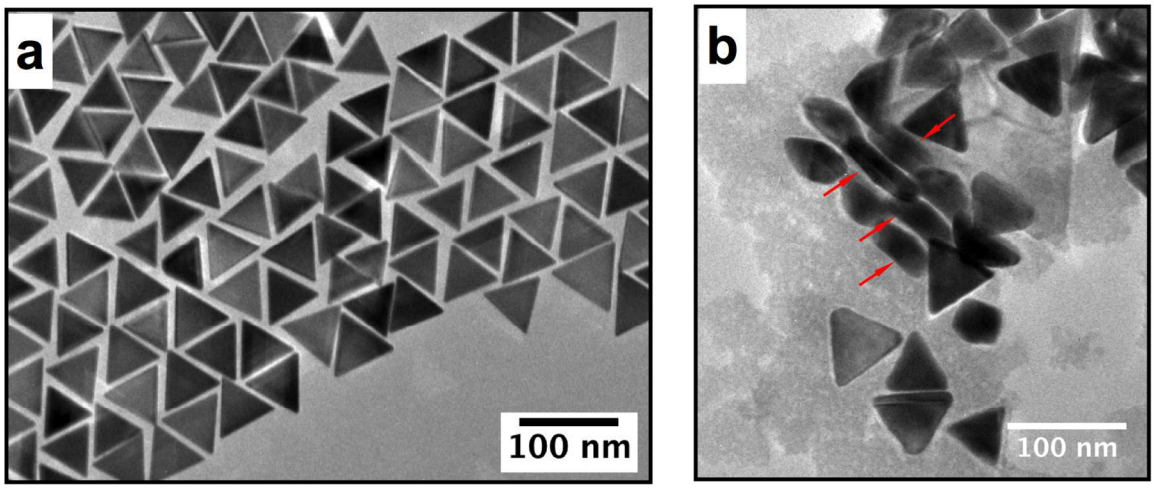

Figure 1. (a) Representative TEM image of PEGylated GNPs. (b) TEM image of GNPs located at different orientation. The red arrows indicate vertically oriented GNPs.

As shown in Figure 2a, spectra of CTAC-capped and PEGylated GNPs peaked at 669 nm, fell into the NIR window. The hydrodynamic diameters of CTAC-capped and PEGylated GNPs were measured, respectively, to be 40.7 ± 1.3 and 42.7 ± 1.6 nm using dynamic light scattering (DLS, Figure 2b). The zeta potential of CTAC-capped GNPs dropped from 24.35 ± 3.49 to 7.40 ± 1.63 mV after PEGylation (Figure 2c). These results suggested the mPEG-SH was successfully attached to the surface of GNPs.

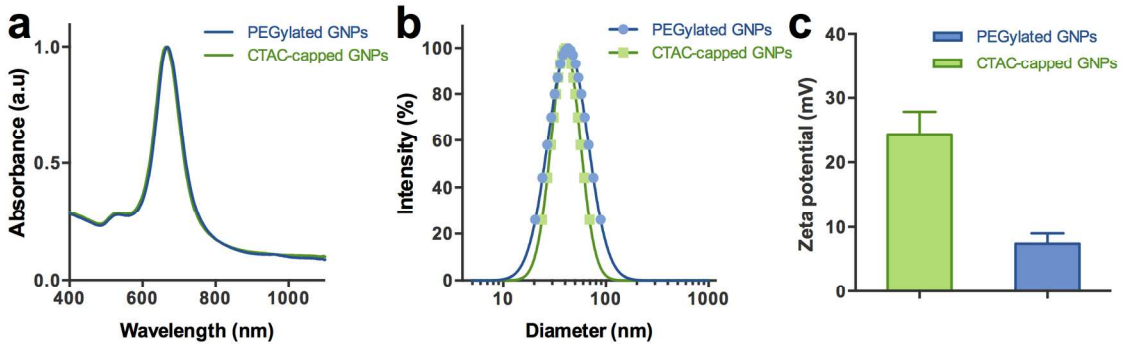

Figure 2. (a) Normalized UV-Vis spectra of CTAC-capped and PEGylated GNPs. (b) Representative DLS distribution of CTAC-capped and PEGylated GNPs. (c) Zeta potential of CTAC-capped and PEGylated GNPs.

It is noted that the DLS distributions of CTAC-capped and PEGylated GNPs are relatively wide despite the small deviation of three independent measurements. To understand the relatively wide distribution of each measurement, we further analyzed the raw data of size distribution. As shown in Figure 3a and 3b, the wide size distribution of CTAC-capped and PEGylated GNPs are actually composed of two narrow distribution peaks. One major particle size distribution peaks around 50-60 nm, the other small particle size distribution peaks around 3-5 nm, which might be mistaken as the presence of small particle impurities. The similar two-peak distribution was also reported in studies of other anisotropic nanoparticles, such as gold nanorods. Recent reports proposed that the small particle distribution is not a real particle size distribution, but a representation of rotational diffusion of anisotropic nanoparticles[22]. Therefore, the small distribution peak indicated that the rotational diffusion coefficient of GNPs is equal to the translation diffusion coefficient of spherical nanoparticles with an average diameter of 3–5 nm. And this small peak made the normalized size distribution of CTAC-capped and PEGylated GNPs appears wide. The low magnification TEM images confirmed the narrow size distribution of GNPs as shown in Figure 1a.

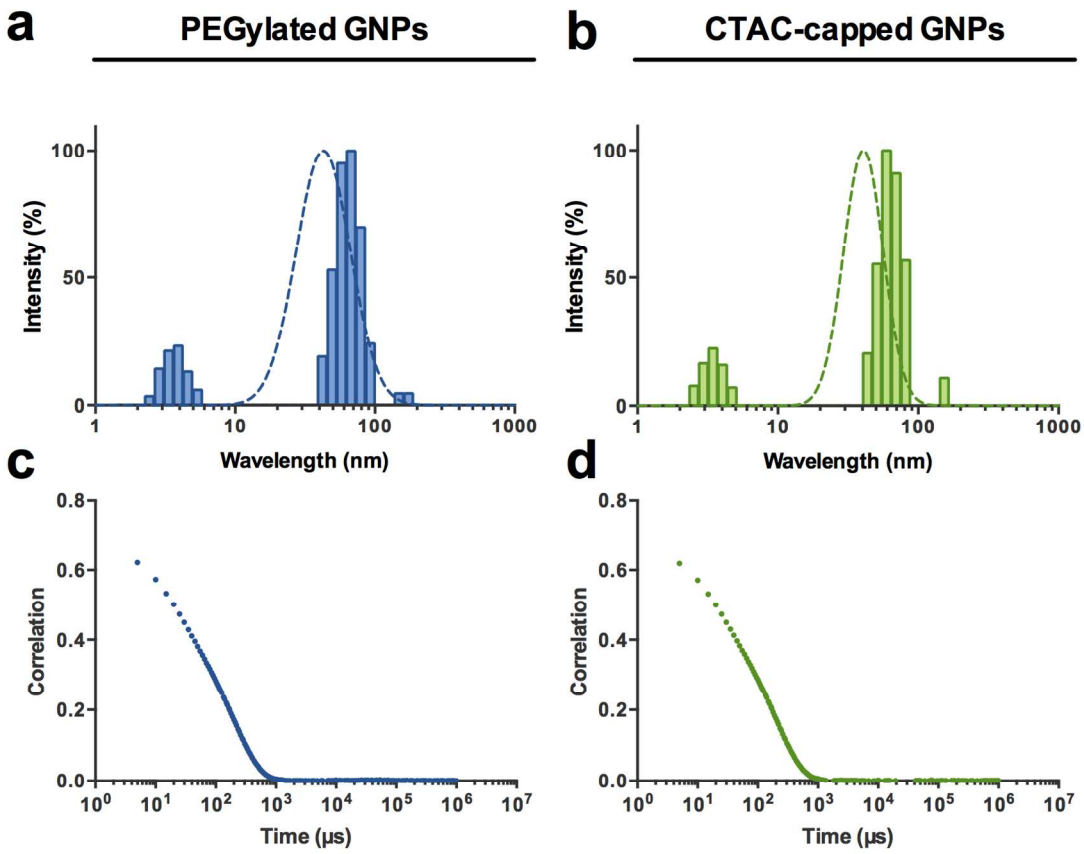

Figure 3. Representative DLS distribution of PEGylated (a) and CTAC-capped GNPs (b) in water. The dash lines represent the normalized DLS distribution. The spikes represent the raw intensity of DLS distribution. DLS distribution of PEGylated (c) and CTAC-capped GNPs (d) reported as the correlation function.

Since the localized surface plasmon resonance is highly sensitive to the shape of nanoparticles, the extinction spectrum of GNPs has been simulated by using the finite-difference time-domain (FDTD) method. As shown in Figure 4, when the edge length and thickness of GNPs were set as 55 and 20 nm, the simulation data was consistent with the experimental result in which the extinction peaked at 679 nm.

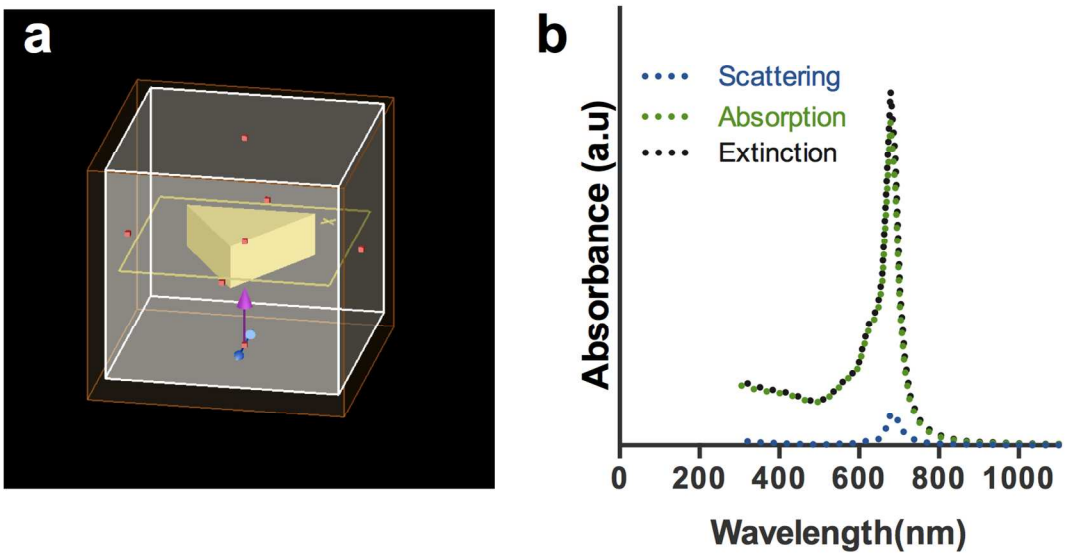

Figure 4. (a) Perspective view of established GNPs model. (b) The scattering, absorption and extinction spectra of GNPs simulated by FDTD solutions.

3.2 photothermal properties of PEGylated GNPs

The photothermal conversion efficacy of PEGylated GNPs was investigated as a function of concentration under NIR laser at 2 W cm^{-2}. Upon irradiation for 10 min, we observed that the maximum equilibrium temperature of the solution gradually increased with the concentration. The solution at 40 μg/mL showed a 39.3 ˚C increase in temperature after irradiation, while no significant change was observed in ultrapure water (Figure 5a). These results demonstrated that PEGylated GNPs generated heat upon NIR laser irradiation with excellent photothermal conversion efficacy. Furthermore, PEGylated GNPs exhibited remarkable photothermal stability under NIR laser irradiation for five cycles (Figure 5b).

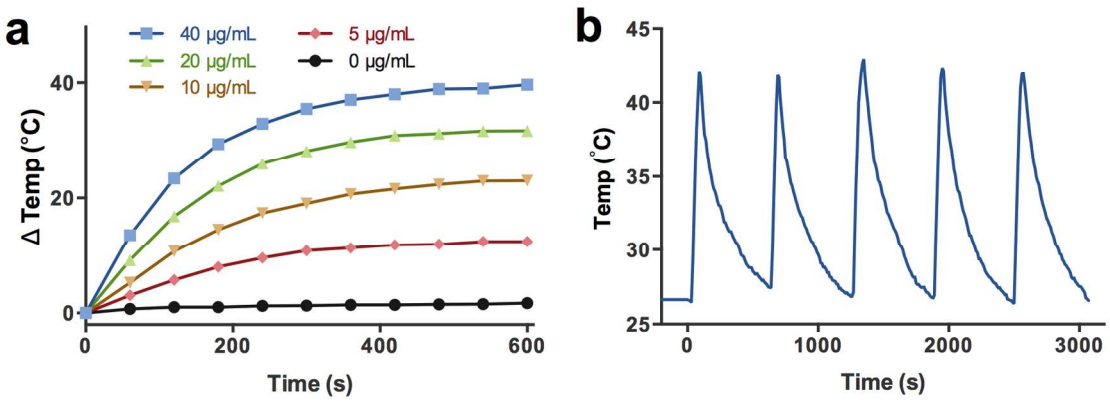

Figure 5. (a) Heating curves of various PEGylated GNPs under laser irradiation at 2 W cm^{-2}. (b) Heating curves of PEGylated GNPs (40 μg/mL) upon laser irradiation at 2 W cm^{-2} for five ON-OFF cycles (ON: 1 min; OFF: 9 min).

The photothermal conversion efficacy of PEGylated GNPs was determined following Roper's report[23] (Figure 6). For PEGylated GNPs at the concentration of 10 μg/mL, the m_{H2O} is 1.0 g and the C_{H2O} is 4.2 J/g/°C, the A is 0.125, $T_{max} - T_{amb}$ is 21.3 °C, I is 2 W, Q_0 is 10.9 mW, τ_s is determined to be 245 sec (Figure 6c), thus the photothermal conversion efficacy (η) of PEGylated GNPs can be calculated to be 70.8%. For PEGylated GNPs at the concentration of 5 μg/mL, $T_{max} - T_{amb}$ is 11.7 °C, τ_s is determined to be 250 sec (Figure 6d), η was calculated to be 69.7%. These results showed that the photothermal conversion efficacy of PEGylated GNPs is independent of the concentration, and significantly higher than many previously reported gold nanostructures, such as gold nanorods (22%),[15] gold nanoshells (13%),[24] and gold nanocages (63%) (summarized in ESI, Table S1).[25] This high photothermal conversion efficacy is likely due to the high absorption to scattering ratio of GNPs according to the simulation result (4b).

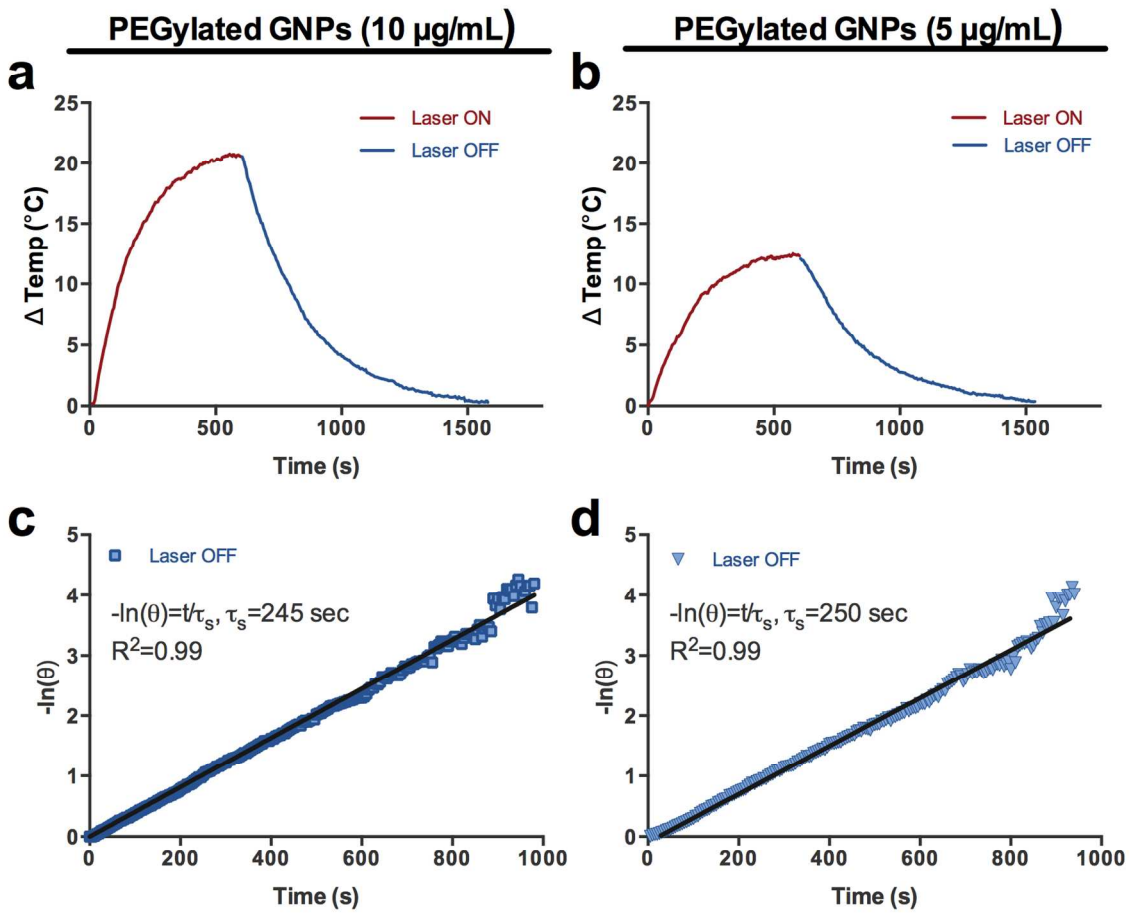

Figure 6. Heating and cooling curves of 10 µg/mL (a) and 5 µg/mL (b) PEGylated GNPs. The laser was lasted for 10 min, and then the laser was turned off. The linear regression between cooling period and negative natural logarithm of driving force temperature of 10 µg/mL (c) and 5 µg/mL (d) PEGylated GNPs.

3.3 Biostability of PEGylated GNPs

To further study the biostability of PEGylated GNPs, PEGylated and CTAC-capped GNPs were centrifuged and re-dispersed in water, PBS, and DMEM (Dulbecco's modified eagle medium, supplemented with 10% serum). As shown in Figure S2, PEGylated GNPs dispersed homogeneously in water, PBS, DMEM, and showed almost the same DLS distribution, while the hydrodynamic diameter of CTAC-capped GNPs

dramatically increased to 1877.7 ± 95.4 nm when dispersed in DMEM (Figure 7a). The UV-Vis measurement also confirmed unchanged absorbance spectra of PEGylated GNPs in DMEM after 24 h of incubation (Figure 7b). These results indicated that the self assembled mPEG layer protected GNPs from nonspecific protein absorption and granted GNPs excellent biostability.

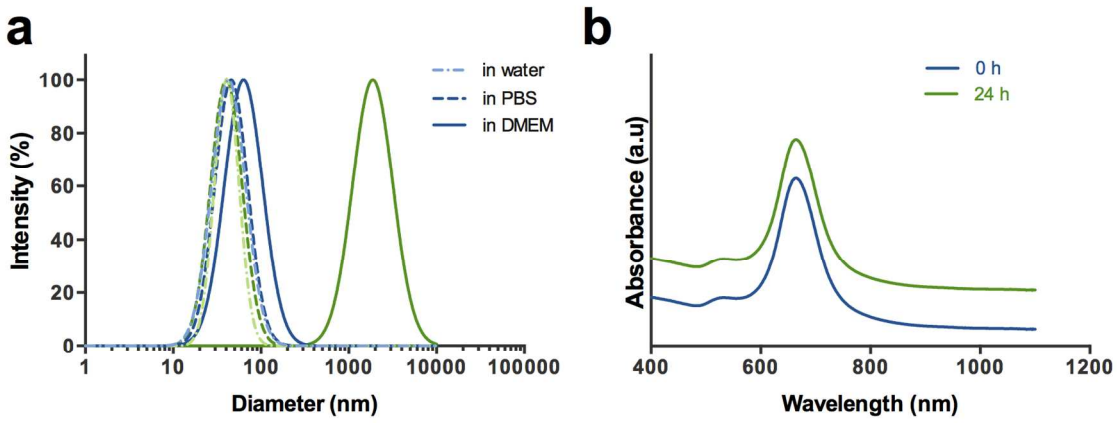

Figure 7. (a) The hydrodynamic diameter distributions of PEGylated GNPs (blue line) and CTAC-capped GNPs (green line) in water, PBS, or DMEM. (b) The UV-Vis absorbance spectra of PEGylated GNPs incubated in DMEM without phenol red for 0 h and 24 h.

3.4 Therapeutic efficacy of PEGylated GNPs

Having demonstrated the ultrahigh photothermal conversion efficacy and biostability of PEGylated GNPs, we next evaluated the therapeutic efficacy of PEGylated GNPs against breast cancer cells upon NIR laser irradiation. The human breast cancer cells (MCF-7 cells) were treated with various concentration of PEGylated GNPs, irradiated by NIR laser (2 W cm^{-2}, 10 min) and followed by a viability assay. As shown in Figure 8, the MTT assay revealed that as the concentration of PEGylated GNPs increased from 2.5 to 80 μg/mL, the viability of the MCF-7 cells decreased from 92.2 ± 6.3% to 5.5 ± 1.4% of

the blank control after laser irradiation. In contrast, negligible toxicity was observed in the MCF-7 cells incubated with PEGylated GNPs without laser irradiation. In addition, the fluorescence live/dead cells staining also agreed well with the MTT assay results.

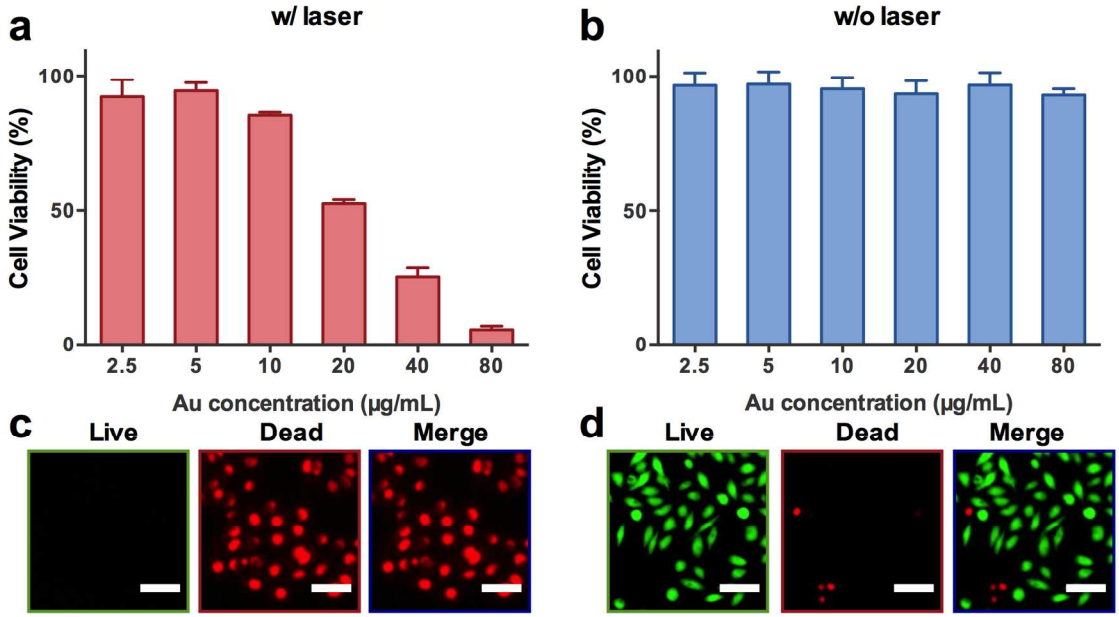

Figure 8. (a) Cell viability of MCF-7 cells incubated with various concentration of PEGylated GNPs for 24 h with laser irradiation (2 Wcm^{-2}, 10 min). (b) Cell viability of MCF-7 cells incubated with various concentration of PEGylated GNPs for 24 h without laser irradiation. The corresponding fluorescence images of calcein AM (green, live cells)/ propidium iodide (red, dead cells) costained MCF-7 cells incubated with 80 μg/mL PEGylated GNPs with (c) or without (d) laser irradiation. Scale bars: 50 μm.

3.5 Biocompatibility of PEGylated GNPs

To determine the potential cytotoxicity of PEGylated GNPs to normal tissues, we next investigated the compatibility of PEGylated GNPs in human breast basal epithelial cells (MCF-10A) and compared that with CTAC-capped GNPs. PEGylated GNPs showed little cytotoxicity to MCF-10A cells even at concentration up to 80 μg/mL, indicating the high biocompatibility of PEGylated GNPs. In contrast, the viability of MCF-10A

dropped from 88.9 ± 3.0 to 4.6 ± 0.5% as the concentration of CTAC-capped GNPs increased from 2.5 to 80 µg/mL (Figure 9a), which is presumably due to the toxicity from surface-attached CTAC.

Hemolysis is an important issue for therapeutic nanoparticles.[26] Therefore, the hemocompatibility of PEGylated GNPs was assessed and compared with CTAC-capped GNPs. Nanoparticle induced hemolysis was not observed on PEGylated GNPs at various concentration, while >90 % hemolytic activity was measured on CTAC-capped GNPs at concentration from 25 to 400 µg/mL (Figure 9b-c).

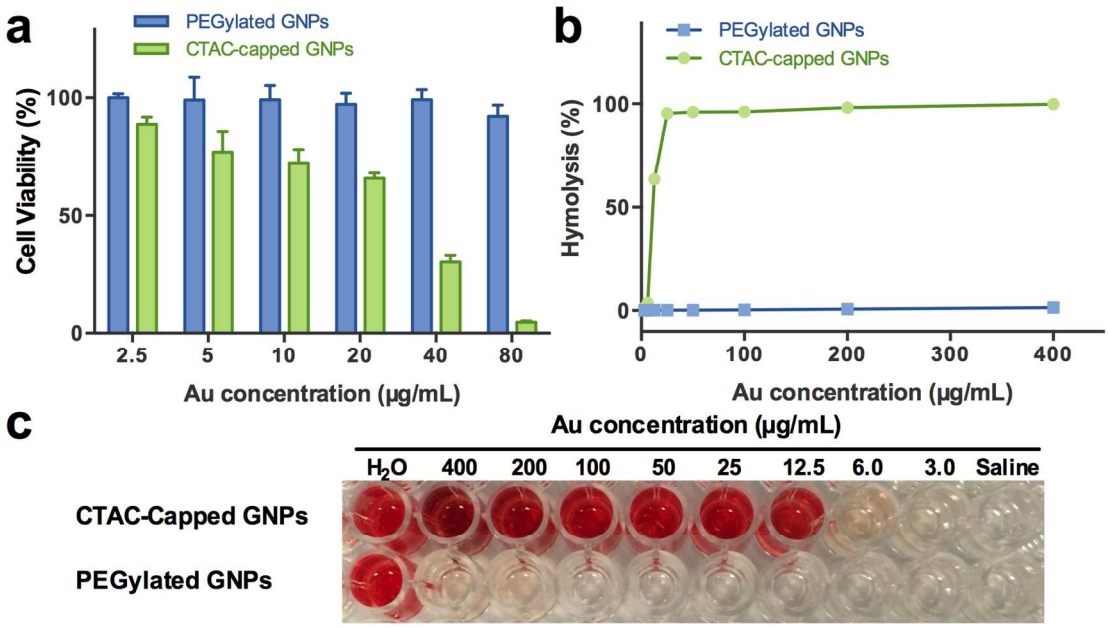

Figure 9. (a) Cell viability of MCF-10A cells incubated with various concentration of CTAC-capped or PEGylated GNPs after 24 h. (b) Hemolytic activity of various concentration of CTAC-capped and PEGylated GNPs. (c) Digital images of GNPs-induced hemoglobin leakage from human erythrocytes after 2 h of exposure to various concentration of CTAC-capped or PEGylated GNPs at 37 °C.

4. Conclusions

In conclusion, this study demonstrated that small-sized PEGylated GNPs can be used for PTT to treat breast cancer at low power density laser. By utilizing ligand exchange process, hydrophilic polymer of PEG can be introduced to the surface of GNPs, and dramatically improved their biostability, biocompatibility and hemocompatibility. We showed that these PEGylated GNPs have high absorbance in NIR window and superior photothermal conversion capacity ($\eta \approx 70\%$) than other gold nanostructure. This is the first demonstration that small-sized PEGylated GNPs can be used as a versatile nanoheater to induce photothermal therapeutic effect at low power density laser (2 W cm^{-2}). Future studies will extend the in vitro concept demonstrated here to in vivo animal experiments.

1 S. Wang, Z. Teng, P. Huang, D. Liu, Y. Liu, Y. Tian, J. Sun, Y. Li, H. Ju, X. Chen and G. Lu, *Small*, 2015, **11**, 1801–1810.
2 S. Wang, P. Huang, L. Nie, R. Xing, D. Liu, Z. Wang, J. Lin, S. Chen, G. Niu, G. Lu and X. Chen, *Adv Mater*, 2013, **25**, 3055–3061.
3 P. Huang, P. Rong, J. Lin, W. Li, X. Yan, M. G. Zhang, L. Nie, G. Niu, J. Lu, W. Wang and X. Chen, *J Am Chem Soc*, 2014, **136**, 8307–8313.
4 A. S. Thakor and S. S. Gambhir, *CA Cancer J Clin*, 2013, **63**, 395–418.
5 L. Cheng, C. Wang, L. Feng, K. Yang and Z. Liu, *Chem Rev*, 2014, **114**, 10869–10939.
6 J. F. Lovell, C. S. Jin, E. Huynh, H. Jin, C. Kim, J. L. Rubinstein, W. C. W. Chan, W. Cao, L. V. Wang and G. Zheng, *Nat Mater*, 2011, **10**, 324–332.
7 Y. Tian, S. Luo, H. Yan, Z. Teng, Y. Pan, L. Zeng, J. Wu, Y. Li, Y. Liu, S. Wang and G. Lu, *J. Mater. Chem. B*, 2015, **3**, 4330–4337.
8 L. Nie, S. Wang, X. Wang, P. Rong, Y. Ma, G. Liu, P. Huang, G. Lu and X. Chen, *Small*, 2014, **10**, 1585–1593.
9 X. Huang, S. Tang, X. Mu, Y. Dai, G. Chen, Z. Zhou, F. Ruan, Z. Yang and N. Zheng, *Nat Nanotechnol*, 2011, **6**, 28–32.
10 N. Khlebtsov and L. Dykman, *Chem Soc Rev*, 2011, **40**, 1647–1671.
11 W. H. De Jong, W. I. Hagens, P. Krystek, M. C. Burger, A. J. A. M. Sips and R. E. Geertsma, *Biomaterials*, 2008, **29**, 1912–1919.
12 R. Weissleder and V. Ntziachristos, *Nat Med*, 2003, **9**, 123–128.
13 Q. Tian, F. Jiang, R. Zou, Q. Liu, Z. Chen, M. Zhu, S. Yang, J. Wang, J. Wang and

J. Hu, *ACS Nano*, 2011, **5**, 9761–9771.
14 K. Yang, H. Xu, L. Cheng, C. Sun, J. Wang and Z. Liu, *Adv Mater*, 2012, **24**, 5586–5592.
15 P. Huang, J. Lin, W. Li, P. Rong, Z. Wang, S. Wang, X. Wang, X. Sun, M. Aronova, G. Niu, R. D. Leapman, Z. Nie and X. Chen, *Angew Chem Int Ed Engl*, 2013, **52**, 13958–13964.
16 L. Chen, F. Ji, Y. Xu, L. He, Y. Mi, F. Bao, B. Sun, X. Zhang and Q. Zhang, *Nano Lett*, 2014, **14**, 7201–7206.
17 G. K. Joshi, K. N. Blodgett, B. B. Muhoberac, M. A. Johnson, K. A. Smith and R. Sardar, *Nano Lett*, 2014, **14**, 532–540.
18 M. Pérez-Hernández, P. Del Pino, S. G. Mitchell, M. Moros, G. Stepien, B. Pelaz, W. J. Parak, E. M. Gálvez, J. Pardo and J. M. de la Fuente, *ACS Nano*, 2015, **9**, 52–61.
19 J. E. Millstone, S. Park, K. L. Shuford, L. Qin, G. C. Schatz and C. A. Mirkin, *J Am Chem Soc*, 2005, **127**, 5312–5313.
20 B. Pelaz, V. Grazú, A. Ibarra, C. Magen, P. Del Pino and J. M. de la Fuente, *Langmuir*, 2012, **28**, 8965–8970.
21 A. Ambrosone, P. Del Pino, V. Marchesano, W. J. Parak, J. M. de la Fuente and C. Tortiglione, *Nanomedicine (Lond)*, 2014, **9**, 1913–1922.
22 H. Liu, N. Pierre-Pierre and Q. Huo, *Gold Bull*, 2012, **45**, 187–195.
23 D. K. Roper, W. Ahn and M. Hoepfner, *J Phys Chem C*, 2007, **111**, 3636–3641.
24 C. M. Hessel, V. P Pattani, M. Rasch, M. G. Panthani, B. Koo, J. W. Tunnell and B. A. Korgel, *Nano Lett*, 2011, **11**, 2560–2566.
25 J. Zeng, D. Goldfeld and Y. Xia, *Angew. Chem. Int. Ed.*, 2013, **52**, 4169–4173.
26 R. P. Rother, L. Bell, P. Hillmen and M. T. Gladwin, *JAMA*, 2005, **293**, 1653–1662.